Available online at www.sciencedirect.com
SCIENCE DIRECT®
International Journal of Heat and Mass Transfer 49 (2006) 1958–1973
International Journal of HEAT and MASS TRANSFER
www.elsevier.com/locate/ijhmt

# Macroscopic thermal properties of real fibrous materials: Volume averaging method and 3D image analysis

J. Lux [a,b,*], A. Ahmadi [a], C. Gobbé [a], C. Delisée [b]

[a] TREFLE UMR 8508, Esplanade des Arts et Métiers, 33405 Talence Cedex, France
[b] LRBB UMR 5103, Domaine de l'Hermitage, 69 route d'Arcachon, 33610 Cestas Gazinet, France

Received 23 December 2004; received in revised form 4 May 2005
Available online 4 January 2006

**Abstract**

A general method combining the volume averaging technique and image analysis is proposed to determine the effective thermal conductivity tensor of real fibrous materials featuring local anisotropic thermal properties. The application of mathematical morphology tools on 3D images of wood based fibrous insulators allows a thorough investigation of the microstructure of these materials. A representative elementary volume is determined and the geometrical structure and local anisotropy are studied and quantified. The classical closure problem coming from the one equation model is solved on the 3D thermal conductivity tensor field and the effective thermal conductivity is computed. Good agreement with available experimental data is achieved.


*Keywords:* Thermal conductivity; Volume averaging method; 3D image analysis; Mathematical morphology; Wood based fibrous materials; Anisotropy

## 1. Introduction

Macroscopic description of heat transfer in a heterogeneous medium may be obtained by the use of up-scaling methods, allowing the definition of a homogeneous medium based on the knowledge of the local properties and geometry of the microstructure. The aim of this paper is to show that the combination of 3D image analysis with the volume averaging technique provides a useful tool to compute the thermal macroscopic properties of real complex materials.

The volume averaging method is, among other upscaling techniques [1], well suited for the determination of macroscopic properties from 3D images of a medium microstructure. It has been extensively used to predict the effective transport properties of heterogeneous ordered or disordered media [2,3]. The macroscopic heat transfer equations are obtained by averaging the local equations within a representative elementary volume (REV). The effective thermal conductivity is expressed in terms of local temperatures integrals. One has to solve a closure problem to map the local temperatures into volume-averaged temperature and thus determine the macroscopic thermal conductivity. Different modelisations may be envisaged depending on the validity of the local thermal equilibrium assumption. When this condition is satisfied, a classical one-equation model [4,5] correctly describes macroscopic heat transfer in a multiphase system. However, the constraints that would determine whether this approach is valid or not have not been clearly identified yet [6,7]. In a more recent study [8], a one-equation model is proposed that does not require an absolute thermal equilibrium. However, there still remains situations in which a single governing equation approach is not satisfactory, thus two- [9], or even three- [10], equations models have been introduced.

Even though the volume averaging method has a solid theoretical background and has been proven to be a robust method, its application to the prediction of macroscopic

* Corresponding author. Address: TREFLE UMR 8508, Esplanade des Arts et Métiers, 33405 Talence Cedex, France. Tel.: +33 (0) 556 845 414; fax: +33 (0) 556 845 401/436.
*E-mail address:* Jerome.lux@bordeaux.ensam.fr (J. Lux).

0017-9310/$ - see front matter © 2005 Elsevier Ltd. All rights reserved.
doi:10.1016/j.ijheatmasstransfer.2005.09.038

**Nomenclature**

| | |
|---|---|
| $A_{\beta\sigma}$ | area of β–σ interface contained in the averaging volume ($m^2$) |
| $A_{\beta e}$ | area of entrances and exits for the β-phase contained within the macroscopic system ($m^2$) |
| $A_{\sigma e}$ | area of entrances and exits for the σ-phase contained within the macroscopic system ($m^2$) |
| $a$ | square root of the wood fibre inner porosity |
| $\mathbf{b}_\beta$ | vector field that maps $\nabla\langle T_\beta\rangle^\beta$ onto $\tilde{T}_\beta$ in the β-phase (m) |
| $\mathbf{b}_\sigma$ | vector field that maps $\nabla\langle T_\sigma\rangle^\sigma$ onto $\tilde{T}_\sigma$ in the σ-phase (m) |
| $C_p$ | specific heat ($J\,kg^{-1}\,K^{-1}$) |
| $g$ | gravitational acceleration ($m^2\,s^{-1}$) |
| $h$ | distance between two points of an image in a given direction (m) |
| $\tilde{\mathbf{K}}_\beta$ | spatial deviation of the conductivity tensor in the β-phase ($W\,m^{-1}\,K^{-1}$) |
| $\tilde{\mathbf{K}}_\sigma$ | spatial deviation of the conductivity tensor in the σ-phase ($W\,m^{-1}\,K^{-1}$) |
| $\mathbf{K}_\beta$ | local conductivity tensor in β-phase ($W\,m^{-1}\,K^{-1}$) |
| $\mathbf{K}_\sigma$ | local conductivity tensor in σ-phase ($W\,m^{-1}\,K^{-1}$) |
| $\mathbf{K}_{eff}$ | macroscopic thermal conductivity ($W\,m^{-1}\,K^{-1}$) |
| $\mathbf{K}_{wf}$ | local thermal conductivity tensor of the wood cell-wall ($W\,m^{-1}\,K^{-1}$) |
| $\langle\mathbf{K}_\beta\rangle^\beta$ | intrinsic β-phase average conductivity tensor ($W\,m^{-1}\,K^{-1}$) |
| $\langle\mathbf{K}_\sigma\rangle^\sigma$ | intrinsic σ-phase average conductivity tensor ($W\,m^{-1}\,K^{-1}$) |
| $K_{long}$ | longitudinal component of the thermal conductivity tensor of homogenized wood fiber ($W\,m^{-1}\,K^{-1}$) |
| $K_{trans}$ | transverse component of the thermal conductivity tensor of homogenized wood fiber ($W\,m^{-1}\,K^{-1}$) |
| $K'_l$ | longitudinal component of the thermal conductivity tensor of wood fibre cell-wall ($W\,m^{-1}\,K^{-1}$) |
| $K'_t$ | transverse component of the thermal conductivity tensor of wood fibre cell-wall ($W\,m^{-1}\,K^{-1}$) |
| $k$ | thermal conductivity ($W\,m^{-1}\,K^{-1}$) |
| $k_{air}$ | thermal conductivity of air ($W\,m^{-1}\,K^{-1}$) |
| $k_{parallel}$ | theoretical thermal conductivity for a parallel arrangement ($W\,m^{-1}\,K^{-1}$) |
| $k_{serial}$ | theoretical thermal conductivity for a serial arrangement ($W\,m^{-1}\,K^{-1}$) |
| $L$ | macroscopic length scale (m) |
| $l_c$ | correlation length (m) |
| $l_i$ | $i = 1, 2, 3$, lattice vectors |
| $l_\beta$ | characteristic length of the β-phase (m) |
| $l_\sigma$ | characteristic length of the σ-phase (m) |
| $N$ | Planck number |
| $p$ | volume fraction of the fibres |
| $P$ | permeability ($m^2$) |
| $Ra^*$ | modified Rayleigh number |
| $T_\beta$ | local temperature in the β-phase (K) |
| $T_\sigma$ | local temperature in the σ-phase (K) |
| $\tilde{T}_\beta$ | spatial temperature deviation in the β-phase (K) |
| $\tilde{T}_\sigma$ | spatial temperature deviation in the σ-phase (K) |
| $\langle T_\beta\rangle$ | average temperature in the β-phase (K) |
| $\langle T_\sigma\rangle$ | average temperature in the σ-phase (K) |
| $\langle T_\beta\rangle^\beta$ | intrinsic β-phase average temperature (K) |
| $\langle T_\sigma\rangle^\sigma$ | intrinsic σ-phase average temperature (K) |
| $\langle T\rangle$ | average temperature (K) |
| $\mathbf{n}_{\beta\sigma}$ | normal unit vector directed from the β-phase to σ-phase (m) |
| $\mathbf{n}_{\sigma\beta}$ | normal unit vector directed from the σ-phase to β-phase (m) |
| $r$ | radius of the averaging volume (m) |
| $\mathbf{r}$ | position vector (m) |
| $t$ | time (s) |
| $V$ | averaging volume ($m^3$) |
| $V_\beta$ | volume of the β-phase contained in the averaging volume ($m^3$) |
| $V_\sigma$ | volume of the σ-phase contained in the averaging volume ($m^3$) |
| $Z$ | empirical factor for reducing the thermal conductive efficiency of the wood fibre cross wall |

*Greek symbols*

| | |
|---|---|
| β | volumetric thermal expansion coefficient of air ($K^{-1}$) |
| $\epsilon_\beta$ | volume fraction of the β-phase contained in the averaging volume |
| $\epsilon_\sigma$ | volume fraction of the σ-phase contained in the averaging volume |
| $\epsilon_{air}$ | volume fraction of the air in insulator materials |
| $\epsilon_{fibres}$ | volume fraction of the fibres in insulator materials |
| $\rho_{air}$ | mass density of air ($kg\,m^{-3}$) |
| $\rho_\beta$ | mass density of the β-phase ($kg\,m^{-3}$) |
| $\rho_\sigma$ | mass density of the σ-phase ($kg\,m^{-3}$) |
| $\mu_{air}$ | dynamic viscosity of air ($kg\,m^{-1}\,s^{-1}$) |

properties of real complex materials is not a trivial task [11]. Difficulties may actually arise when determining the local properties fields, or when one has to choose an averaging volume which satisfies the length and representativeness constraints required by the averaging process.

In this work, we are interested in studying fibrous materials and predicting their macroscopic thermal properties. These materials often present anisotropies that appear at different scales. The local physical properties may indeed depend on the local orientation of the fibres, and the fibres

arrangement may be strongly anisotropic at the macroscopic scale.

Two wood fibres based materials, intended for building insulation, are considered in this study. The first one is a wood/polymer composite featuring 20% of polymer fibres and 80% of wood fibres, in fibres volume fraction, with a very low density of 0.045. The other insulator is exclusively wood based and presents a higher density (0.17). Visualization of these materials by X-ray tomography reveals a rather complex and anisotropic microstructure. Furthermore, wood fibres cover a wide range of diameters, lengths and inner porosities. In addition, as we will see later, the fibres present an orthotropic local thermal conductivity. This makes local orientation an important parameter.

In the first part of this paper, we show that image analysis tools coming from mathematical morphology concepts [12–15] allow a thorough investigation of the microstructure. Some measurements are realized in order to find a representative elementary volume. The study of the anisotropy is done through the use of covariograms and local orientations computation. We will show that these tools allow a good quantification of the medium anisotropy.

In the second part, the averaging process is described. Two steps are involved; first, the wood fibres are homogenized using measured values of the fibres porosity and the local orientations field. Then, the averaging method is applied on the previously defined representative elementary volume. The particular discretization method used to deal with full tensor equations that arise in the closure problems is also described. Numerical results are finally compared to the experimental data obtained by hot-wire and hot-strip methods [16].

## 2. Microstructure characterization

Three dimensional images of wood fibres based insulators are realized using X-ray tomography by absorption at the ESRF (European Synchrotron Radiation Facility) in Grenoble (France). Resolution of images is chosen to be 4.91 μm/pixel, in order to visualize wood fibres inner porosity and to obtain reasonable accuracy for the smallest fibres (diameter around 20 μm). The samples are cylinders with height and diameter of about 1 cm, leading to rather large grey level images of $2048^3$ voxels. Smaller volumes are then extracted from the raw image in the core of the sample, to avoid surface modifications induced by the material cutting.

Details about tools used for the following image processing and analysis are not provided here, as they call upon concepts from mathematical morphology theory, which is beyond the scope of this paper. See [17] for a brief overview of tools and applications and [12–15] for more extensive and theoretical reviews. Here, we will only describe briefly the main steps involved in the image processing.

First, the noise is removed in the raw grey level images using an *opening by reconstruction* [18], which suppresses small particles without modifying the dynamics of the contours. The next step consists of image segmentation, i.e. identification of the different phases. A threshold value is chosen according to the grey level histogram and the expected porosities of the materials. A binary image is then obtained featuring only two phases, fibres and air. Fig. 1 presents the effect of the filtering and segmentation process on a longitudinal section of the wood/polymer composite insulator. Fig. 2 represents the 3D visualization of the sample.

Finally, 3D informations can be extracted from the segmented image. In this section, the wood fibres porosity, which is a key parameter for the fibres homogenization, is computed. Then, the effect of the size of the treated volume over various measurements is studied. A representative elementary volume is proposed, based on the constraints inherent to the averaging method. At last, local

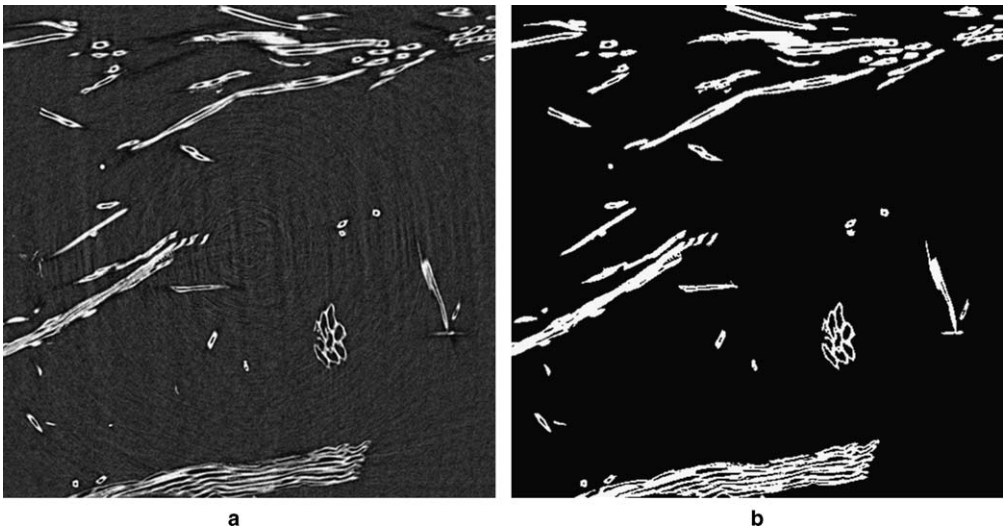


Fig. 1. Longitudinal section before (a) and after (b) image filtering and segmentation.

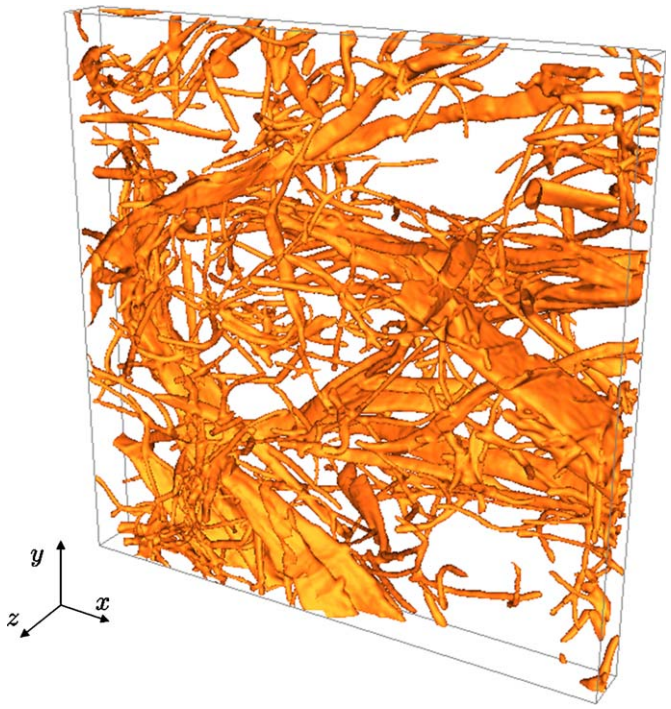


Fig. 2. Visualization of a binary sample of size $5 \times 5 \times 0.6\ \text{mm}^3$.

orientations of the fibres are computed, which allow a thorough analysis of the material anisotropy. In this study, both materials are characterized in the same way, but only results and figures concerning the wood/polymer composite material are presented.

### 2.1. Wood fibres porosity

Wood fibres present an inner porosity, called lumen, in which the sap flows through when a tree is alive. A mean value of inner porosity may be evaluated by a simple measurement of the image volume (i.e. number of voxels) before and after lumens filling. Lumens are filled using morphological operations: first, a *closing* is performing in order to disconnect the fibres porosity from the outer porosity and then, a *closing by reconstruction* fills the fibres remaining inner porosity.

Fig. 3 illustrates the filling process on a longitudinal section of a fibre. A fibre porosity of 26% is computed for the two studied materials, which is in good agreement with values given by [19].

### 2.2. Averaging volume determination

The application of the volume averaging method requires that some length scale constraints be satisfied [9]. Indeed, the averaging volume size has to be large compared to the local heterogeneities and small compared to the macroscopic scale. The choice of a REV is often based on the study of one parameter like the porosity, and usually there is no study of other geometrical, morphological or topological aspects. While this may not be necessary with a medium with calibrated geometry, it is very important to carefully characterize the microstructure in the case of real anisotropic random materials.

In practice for a two-phase medium ($\beta$ and $\sigma$) the following length scale constraints have to be verified:

$$l_\beta, l_\sigma \ll r \ll L \tag{1}$$

The idea behind these length scale constraints is that the averaging volume has to be a representative elementary volume. It should be sufficiently large so that it contains all the geometrical features of the whole medium. Also, when dealing with a non-periodic medium, the periodic boundaries conditions used to solve the closure problems require that results obtained within a periodic cell be representative of the whole material. Intuitively, we can assume that this behaviour may be achieved when the correlation length $l_c$ is much smaller than the REV's dimensions. It should be noted that the length scale constraint may dramatically vary with the medium geometry and the studied process. Therefore, it is difficult to get estimates on a given problem before performing numerical experiments. If we refer to the literature, estimates like $r \sim 10 l_c$ are often considered [20,21], which give us an order of magnitude. An interesting analysis of the influence of size and shape of the averaging volume on the geometrical spatial moments of disordered media may be found in [22,23]. However, it has been found that the stabilization of the spatial moments does not imply that the considered volume is a REV. Here, our aim is to show that a REV may be estimated with respect to the stabilization of various geometrical features like porosity, pores size distribution, fibres diameter distribution and correlation lengths estimates.

On the practical side, the images may be downsampled to a 9.82 μm/pixel and even 19.64 μm/pixel resolution in order to make the size of the images compatible with the memory and computing time constraints, when working


Fig. 3. Example of a fibre section before (a) and after (b) lumen filling.

on large volumes. Special care is taken so that the connexity and porosity remain close at different resolutions. It is worth mentioning that a connexity study has been performed though not presented here. It has been shown that the fibre network is almost entirely connected, even when small volumes are considered.

*2.2.1. Real porosity*

The porosity values measured on the composite insulator for different volume sizes are plotted in Fig. 4. The porosity is stabilized from small volumes around 4 $(2.5 \times 2.5 \times 0.6)$ mm$^3$ and slightly fluctuates around a mean value of 93.4%, which is the same as the porosity measured on the whole sample.

*2.2.2. Size of the pores and of the fibres*

The size distribution of the fibres and of the pores can be assessed performing, respectively on the set of the fibres and of the pores, successive *openings* by spheres and cubes. It is referred in the literature as a *granulometry by openings* [13].

First, a granulometry performed on the set of the fibres allows the measurement of the distribution of their diameters. Granulometric curves are reported in Fig. 5 for different sizes of the treated volumes. We may remark that a size of 31.8 $(5 \times 5 \times 1.26)$ mm$^3$ is required to include the wood chips with diameters larger than 200 μm. One may however notice that this class of fibres represent less than 2% of the fibres volume, thus their importance in the heat transfer

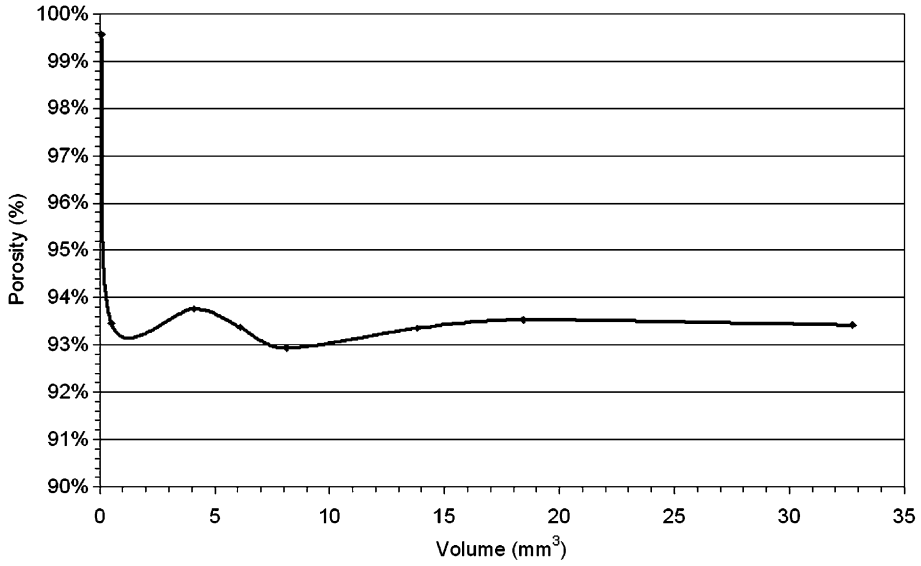


Fig. 4. Evolution of porosity with the size of the treated volume.

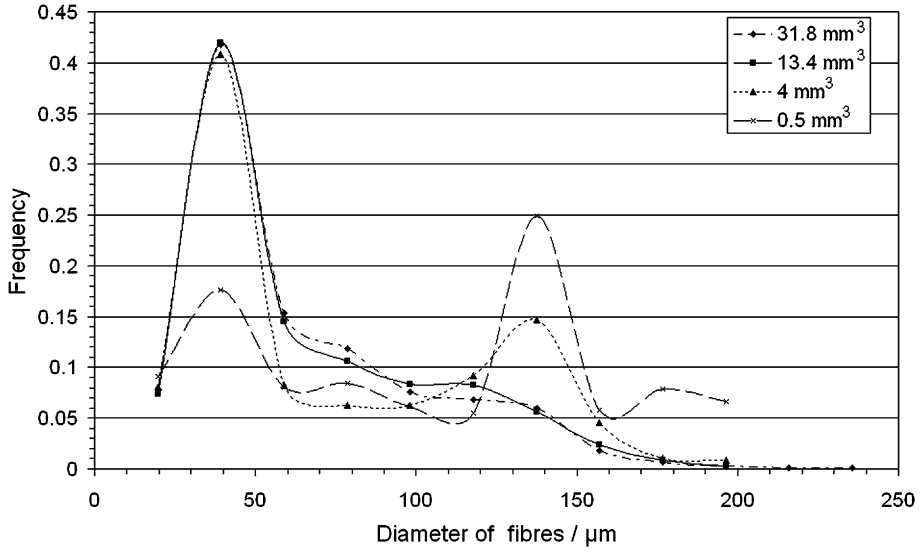


Fig. 5. Distribution of the diameter of the fibres.

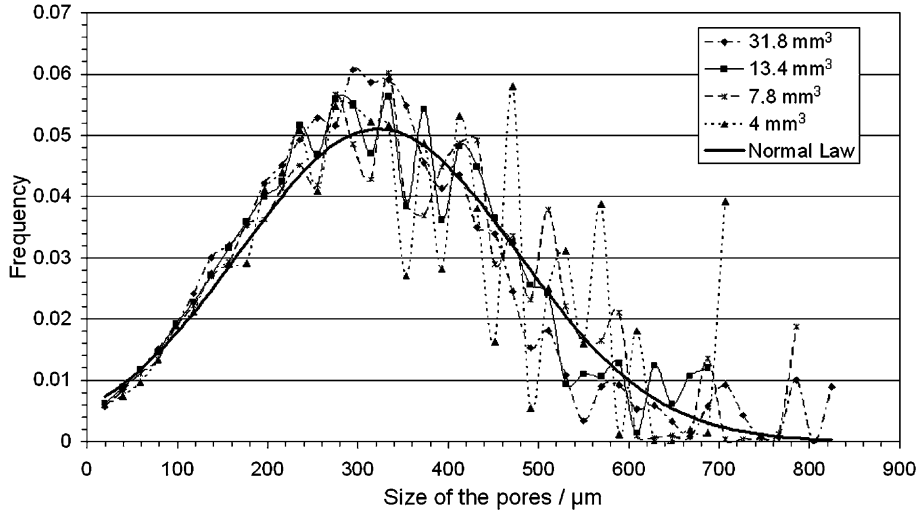


Fig. 6. Evolution of the size of the pores distribution with the size of the treated volume.

process may be questionable. If we choose to ignore them, the stabilization of the distribution occurs at a much smaller volume size of 13.4 ($3.8 \times 3.8 \times 0.93$) mm$^3$. The mean fibre diameter computed on the largest volume is 64.8 μm with a standard deviation of 37 μm.

Then, the pore size distribution can be achieved in a similar manner. However, considering the high connectivity of the pores and their varied shapes, a granulometry performed on the set of the pores informs us more on the inter fibres distance than on a real pores size distribution. The influence of the size of the treated volume on the distribution is shown in Fig. 6. A gaussian curve is also plotted, with mean (322 μm) and variance (153 μm) computed from the distribution measured on the largest volume (31.4 ($5 \times 5 \times 1.26$) mm$^3$). One can note that the larger the volume is, the closer the distribution is to a gaussian curve. These results are a strong indication of the random nature of the fibres arrangement. It seems that the distribution is reasonably close to the gaussian curve from a volume of 13.4 ($5 \times 5 \times 1.26$) mm$^3$.

### 2.2.3. Structure analysis

The study of the spatial distribution of the phases may be realized by computations of the *non-centered covariance*, which is defined as the probability for two points to belong to the same phase [13,14]. From this definition, covariance may be used to evaluate correlation length. Covariograms, i.e. representations of covariance along defined orientations, are also useful to detect anisotropy of the whole structure.

Covariograms are computed on several directions contained in the three planes $xOy$, $xOz$ and $yOz$ (expressed in spherical notations $\{\theta, \varphi\}$, see Fig. 7), on a sample of size 31.8 ($5 \times 5 \times 1.26$) mm$^3$. The variable h represents here the distance between two points in a given direction. The covariograms for all directions are presented in the Fig. 8. These curves indicate the anisotropy of the structure. Indeed, it seems that the fibres are contained globally in planes parallel to the $xOy$ plane ($\varphi = 0$), and orientated especially along the $Ox$ axis (corresponding to an angle of $\{0°, 0°\}$). This result was in fact expected since the material is compressed along the $Oz$ direction during the manufacturing process.

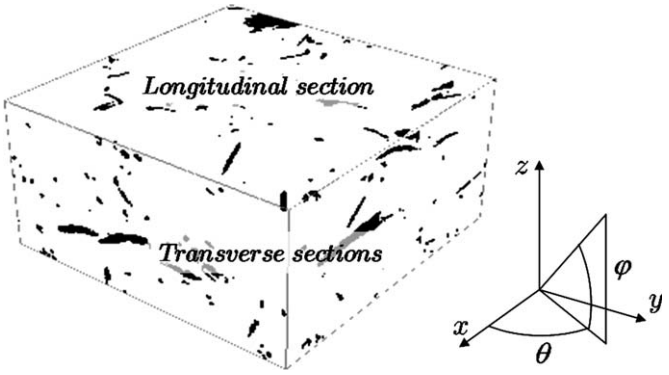


Fig. 7. Angular notations.

When the correlation between two points vanishes, the non-centered covariance tends to an asymptote of equation $y = p^2$, where $p$ is the volume fraction of fibres [12]. The correlation lengths may therefore be estimated when the covariance curves come close to the asymptote. The correlation length values for the tested directions are evaluated between around 0.5 mm and 0.9 mm, corresponding respectively to transverse and longitudinal directions.

### 2.2.4. Conclusion

In this section, the effect of the size of the treated volume over various geometrical features of a sample was studied. An asymptotic behaviour was observed thus proving the existence of a REV for the measured properties. Actually, only numerical computations will tell if this volume is also

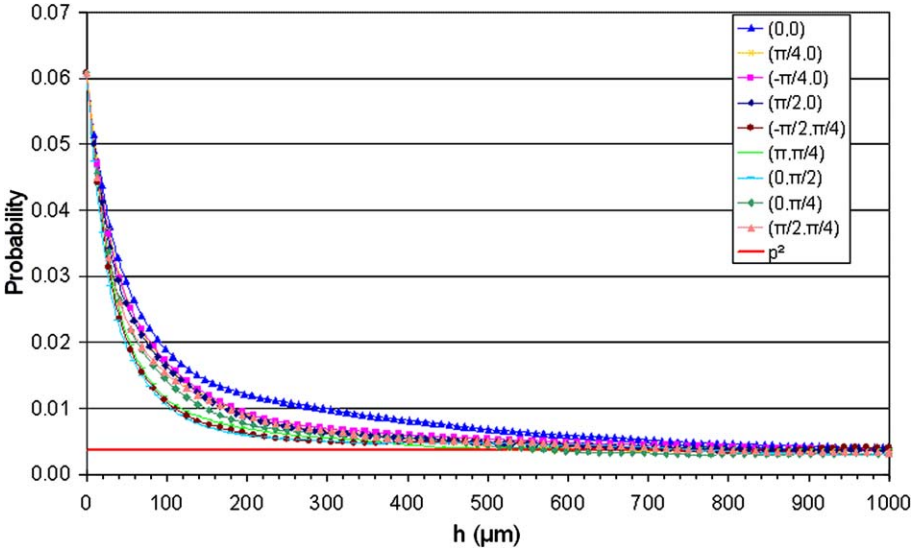


Fig. 8. Experimental covariograms for all tested directions.

representative for the heat transfer process, and thus may validate this analysis. Sufficient representativeness for the measured geometrical parameters is achieved within a volume larger than 13.4 ($2.5 \times 2.5 \times 0.93$) mm$^3$.

The expected anisotropy of the fibrous network is confirmed by the study of covariograms. Finally, the correlation lengths are found to be smaller than the size of the chosen REV, even if the constraint $r \sim 10 l_c$ is not satisfied. The averaging method has, however, been proven to be quite robust regarding this constraint and particularly in the case of purely diffusive processes [11].

### 2.3. Local directions

The up-scaling process requires the knowledge of the local physical properties of the studied material. As we mentioned earlier, the wood fibres present orthotropic thermal conductivity. It is therefore necessary to know the local directions of the fibres to be able to define the principal axis of the local conductivity tensor.

In order to find the longitudinal direction of a voxel of a fibre, a new definition based on morphological *openings* is proposed for multi-scale binary images. The description of this tool is beyond the scope of this paper and will not be discussed here. The developed algorithm allows the detection of the local orientations in the 13 directions that do not introduce any bias in the *cubic lattice*, leading to a step of $\frac{\pi}{4}$ for the angles $\theta$ and $\varphi$. This choice is made in this first attempt to avoid discretization errors, and to reduce the computing time, which is an important parameter when working with large 3D images.

A field of local directions computed on a simple 2D image, for the sake of clarity, is presented in Fig. 9, with 4 identifiable directions. The local directions fields are computed relatively quickly even on large 3D images since only simple morphological operations are required.

Fig. 9. Local directions field on a 2D test image.

The distribution of the local orientations can be assessed from the computed fields. The volume fractions of the fibres for each tested direction, measured on a sample with a size of 31.8 ($5 \times 5 \times 1.26$) mm$^3$, are reported in Fig. 10. This analysis supplements the study of the covariograms by the mean of local informations. The anisotropy of the sample is here very well identified and quantified, as more than 60% of the fibres voxels are oriented on longitudinal planes (parallel to $xOy$) and only 1% is along the transverse direction (along the $z$-axis).

The heat transfer model may now be developed with the help of all the results presented in this section.

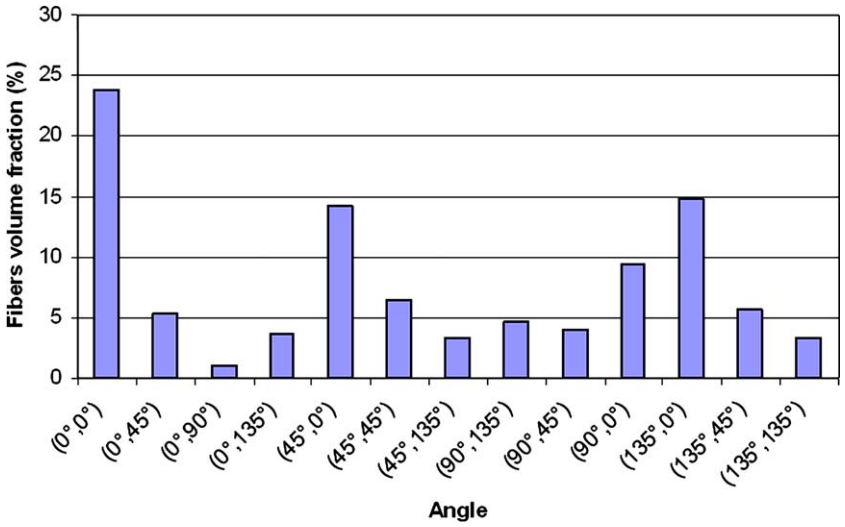


Fig. 10. Distribution of the local orientations.

## 3. Macroscopic model for heat transfer in porous media

### 3.1. Wood fibres thermal conductivity

As previously mentioned, the thermal conductivity of the wood cell-wall is orthotropic:

$$\mathbf{K}_{\mathrm{wf}} = \begin{bmatrix} K'_{\mathrm{l}} & 0 & 0 \\ 0 & K'_{\mathrm{t}} & 0 \\ 0 & 0 & K'_{\mathrm{t}} \end{bmatrix} \tag{2}$$

Values of $K'_{\mathrm{l}} = 0.88\ \mathrm{W\,m^{-1}\,K^{-1}}$ for the longitudinal component and $K'_{\mathrm{t}} = 0.44\ \mathrm{W\,m^{-1}\,K^{-1}}$ for the transverse components are well identified [24]. However, the wood cell-wall may be distinguished from the lumen only at a sufficiently high resolution. The use of high resolution images is not compatible with the size of the REV, as it would impose too large memory requirement and extensive computation times. Therefore, lower resolutions have to be considered. As a consequence, values of thermal conductivities have to be known for filled fibres. This step constitutes a first up-scaling process for the wood fibres. A model derived by [24] is chosen to homogenize the wood fibres thermal conductivity, which depends on the fibres porosity. In this approach, the main drawback is that a fibre is supposed to have a simple geometric structure, as presented in Fig. 11a. The parameter $a$ is the square root of the fibre porosity. The longitudinal conductivity component is then easily expressed as

$$K_{\mathrm{long}} = K'_{\mathrm{l}}(1 - a^2) + k_{\mathrm{air}} a^2 \tag{3}$$

The transverse conductivity is more complex to obtain, and the chosen conductivity model is depicted in Fig. 11b. The factor $Z$ is introduced to reflect that the entire cross-wall (parts of the cell-wall perpendicular to the heat flux) is not effective for conduction. $Z$ is determined from experimental data ($Z = 0.72$) and the empirical relation is given in [24]. The transverse conductivity is then

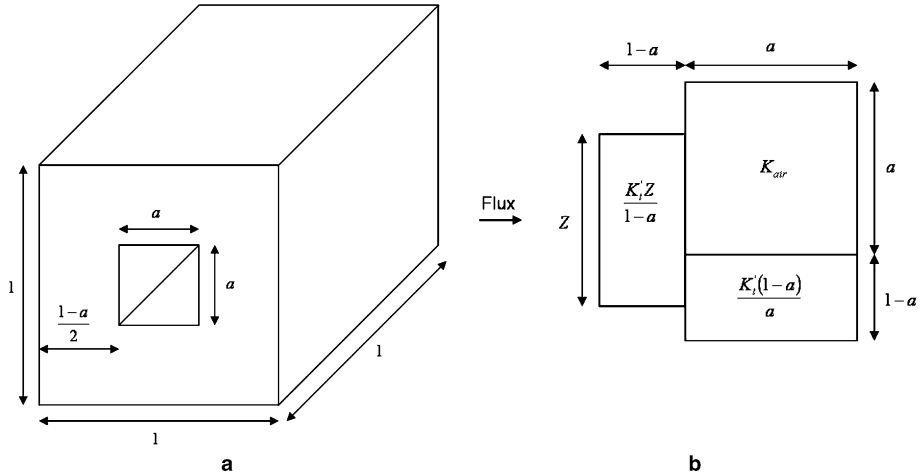


Fig. 11. Geometrical model for a wood fibre (a) and transverse conductivity model (b) described in [24].

$$K_{\text{trans}} = \frac{(1-a)ZK_{\text{t}}'^2 + aZk_{\text{air}}K_{\text{t}}'}{(1-a)^2K_{\text{t}}' + a(1-a)k_{\text{air}} + aZK_{\text{t}}'} \quad (4)$$

Values of $K_{\text{long}} = 0.66\ \text{W m}^{-1}\ \text{K}^{-1}$ and $K_{\text{trans}} = 0.3\ \text{W m}^{-1}\ \text{K}^{-1}$ are calculated with the previously measured wood fibres porosity of 26%. Using these values in conjunction with the local directions field allows to define the local thermal conductivity field. On a side note we may add that the polymer fibres thermal conductivity, which is isotropic and around $0.3\ \text{W m}^{-1}\ \text{K}^{-1}$, is the same as the transverse conductivity for the wood fibres. The local longitudinal component is thus overestimated when assimilating polymer fibres to wood fibres. However, the fact that the polymer fibres represent around only 20% of the fibres volume fraction (and thus only between 1% and 2% of the volume of the REV), is an indication that the error committed is a priori small regarding the macroscopic conductivity.

### 3.2. Conductive, convective and radiative contributions

In this work, only diffusive heat transfer is considered. This choice of neglecting convective and radiative heat transfer may seem to be a strong assumption in this kind of high porosity materials. A study of appropriate dimensionless numbers is proposed to justify this approach.

In order to evaluate the relative importance of the convective heat transfer, the modified Rayleigh number $Ra^*$ [25] is calculated:

$$Ra^* = \frac{g\beta\rho_{\text{air}}^2}{\mu_{\text{air}}} \times \frac{P}{k} \times \Delta T \times L \quad (5)$$

where $g$ is the gravitational acceleration ($\text{m}^2\ \text{s}^{-1}$), $\beta$ is the volumetric thermal expansion coefficient of air ($\text{K}^{-1}$), $\rho_{\text{air}}$ is the air mass density ($\text{kg m}^{-3}$), $P$ is the permeability ($\text{m}^2$), $\Delta T$ is the temperature difference (K) between the two sides of the sample, $L$ is the material thickness (m), $\mu_{\text{air}}$ is the dynamic viscosity of air ($\text{kg m}^{-1}\ \text{s}^{-1}$) and $k$ is the thermal conductivity $\text{W m}^{-1}\ \text{K}^{-1}$.

The convective heat flow may be ignored if $Ra^*$ is less than 40. The values of $\Delta T = 25$ K for the temperature difference and $L = 0.25$ m for the thickness are chosen so that they correspond to real use conditions, which are far more favorable concerning the apparition of convection than the experimental conditions. The conductivity value of $0.05\ \text{W m}^{-1}\ \text{K}^{-1}$ comes from experimental data. The value of permeability is calculated by the Kozeny-Carman equation [26] leading to an estimate of $4.5 \times 10^{-9}\ \text{m}^2$. Even with these conditions the modified Rayleigh number is close to 1 so convection may be neglected with confidence regarding conduction.

Concerning the radiative contribution, it is intuitively appealing to consider it negligible since the material is to be used at low temperature, typically below 293 K. One may calculate the Planck number $N$ in order to evaluate the importance of radiative transfer over conduction [27]:

$$N = \frac{k}{4n^2\sigma T^3 l_{\text{p}}} \quad (6)$$

where $l_{\text{p}}$ is the mean free path of photons, $n$ is the refractive index of air ($n = 1$) and $\sigma$ is Stephan's constant ($5.68 \times 10^{-8}\ \text{W m}^{-2}\ \text{K}^{-4}$). If we assume that the mean free path of photons is equivalent to the mean inter-fibre distance, computed previously (322 μm), then $N = 27$ at $T = 293$ K. Since $N > 10$, the radiative transfer may be neglected regarding conduction.

Keeping these considerations in mind, we are now in a position to move on to the development of a purely conductive macroscopic heat transfer model.

### 3.3. Volume averaging method

#### 3.3.1. Heat transfer equations

The governing differential equations and boundary conditions for transient conductive heat transfer in a medium constituted by two phases σ and β, assuming that $\rho C_{\text{p}}$ is constant in each phase, are given by

$$(\rho C_{\text{p}})_\beta \frac{\partial T_\beta}{\partial t} = \nabla \cdot [\mathbf{K}_\beta \cdot (\nabla T_\beta)] \quad \text{in the } \beta\text{-phase} \quad (7)$$

$$T_\beta = T_\sigma \quad \text{on } A_{\beta\sigma} \quad (8)$$

$$\mathbf{n}_{\beta\sigma} \cdot \mathbf{K}_\beta \cdot \nabla T_\beta = \mathbf{n}_{\beta\sigma} \cdot \mathbf{K}_\sigma \cdot \nabla T_\sigma \quad \text{on } A_{\beta\sigma} \quad (9)$$

$$(\rho C_{\text{p}})_\sigma \frac{\partial T_\sigma}{\partial t} = \nabla \cdot [\mathbf{K}_\sigma \cdot (\nabla T_\sigma)] \quad \text{in the } \sigma\text{-phase} \quad (10)$$

$$T_\beta = \mathscr{F}(\mathbf{r}_\beta, t) \quad \text{on } A_{\beta\text{e}} \quad (11)$$

$$T_\sigma = \mathscr{G}(\mathbf{r}_\sigma, t) \quad \text{on } A_{\sigma\text{e}} \quad (12)$$

It is also useful to recall here some definitions of the notations used in the volume averaging method:

The average $\langle \Psi_i \rangle$ of a quantity $\Psi_i$ defined in the phase $i$ is given by

$$\langle \Psi_i \rangle = \frac{1}{V} \int_{V_i} \Psi_i \, \text{d}V \quad (13)$$

and the intrinsic phase average $\langle \Psi_i \rangle^i$ may be expressed as

$$\langle \Psi_i \rangle^i = \frac{1}{V_i} \int_{V_i} \Psi_i \, \text{d}V = \frac{1}{\epsilon_i} \langle \Psi_i \rangle \quad (14)$$

It is also supposed that $\Psi_i$ may be expressed as the sum of its intrinsic phase average and a local deviation term:

$$\Psi_i = \langle \Psi_i \rangle^i + \tilde{\Psi}_i \quad (15)$$

where the average of the local deviation is assumed to be zero, provided that the constraints (1) are satisfied [22,23]:

$$\langle \tilde{\Psi}_i \rangle \simeq 0 \quad (16)$$

The average operator is applied over Eqs. (7) and (10), then the use of the averaging theorem [28] leads to the following equations:

$$\epsilon_\beta(\rho C_p)_\beta \frac{\partial\langle T_\beta\rangle^\beta}{\partial t} = \nabla\cdot\left(\langle \mathbf{K}_\beta\rangle^\beta\cdot\left(\epsilon_\beta\nabla\langle T_\beta\rangle^\beta + \frac{1}{V}\int_{A_{\beta\sigma}}\mathbf{n}_{\beta\sigma}\tilde{T}_\beta\,dA\right) + \langle\tilde{\mathbf{K}}_\beta\cdot\nabla\tilde{T}_\beta\rangle\right) + \frac{1}{V}\int_{A_{\beta\sigma}}\mathbf{n}_{\beta\sigma}\cdot\mathbf{K}_\beta\cdot\nabla T_\beta\,dA \quad (17)$$

in the β-phase and

$$\epsilon_\sigma(\rho C_p)_\sigma \frac{\partial\langle T_\sigma\rangle^\sigma}{\partial t} = \nabla\cdot\left(\langle \mathbf{K}_\sigma\rangle^\sigma\cdot\left(\epsilon_\sigma\nabla\langle T_\sigma\rangle^\sigma - \frac{1}{V}\int_{A_{\beta\sigma}}\mathbf{n}_{\beta\sigma}\tilde{T}_\sigma\,dA\right) + \langle\tilde{\mathbf{K}}_\sigma\cdot\nabla\tilde{T}_\sigma\rangle\right) - \frac{1}{V}\int_{A_{\beta\sigma}}\mathbf{n}_{\beta\sigma}\cdot\mathbf{K}_\sigma\cdot\nabla T_\sigma\,dA \quad (18)$$

in the σ-phase.

Now, we have to decide whether thermal equilibrium may be assumed or not. It is interesting to note that the choice of one- or two-equation model is also a choice of a time scale. Indeed, in the case of purely diffusive heat transfer, one may always choose a sufficiently long time $t$ so that thermal equilibrium is achieved. In the case of building insulation, the material is not subject to rapid temperature variations, and it is assumed that the transient heat transfer is fast enough so that local thermal equilibrium may be considered as valid. Furthermore, the contrast of conductivity between the phases is not high, as the ratio $k_{wood}/k_{air}$ is about 10. It is shown in [6] that the contrast is another factor that influences the thermal equilibrium. A one-equation model is thus chosen in a first approach. However, numerical experiments should be done in order to understand the influence of the day/night periodic solicitations over the thermal equilibrium assumption.

If we assume that the local thermal equilibrium assumption is valid, then, the two intrinsic phase average temperatures may be considered sufficiently close so that a one temperature model may be developed. The average temperature is

$$\langle T\rangle = \frac{1}{V}\int_{V_\beta} T_\beta\,dV + \frac{1}{V}\int_{V_\sigma} T_\sigma\,dV = \epsilon_\beta\langle T_\beta\rangle^\beta + \epsilon_\sigma\langle T_\sigma\rangle^\sigma \quad (19)$$

Keeping in mind that we deal with macroscopic quantities, the local thermal equilibrium condition yields

$$\langle T_\beta\rangle^\beta \simeq \langle T_\sigma\rangle^\sigma \quad (20)$$

then it is evident from (19) that we have

$$\langle T\rangle \simeq \langle T_\beta\rangle^\beta \simeq \langle T_\sigma\rangle^\sigma \quad (21)$$

Here, the temperature to be used in the model is simply the average temperature, but other authors [8] derive the temperature from the average of the enthalpy. They showed that both the volume averaging and homogenization method lead to the same one-equation model that does not require an absolute thermal equilibrium (which may not be achieved when convective transfer is considered). However, without convective transfer, the two formulations of the average temperature yield the same results in term of effective conductivity tensor and closure problems. In the case where the two intrinsic phase average temperatures are not close enough, a two-equation model should eventually be used.

A great amount of work is available in the literature on the derivation of the one equation model and we refer the reader to [3,4,9] for a comprehensive study, as it will not be developed here.

The addition of Eqs. (17) and (18) leads to the macroscopic equation:

$$\langle\rho C_p\rangle\frac{\partial\langle T\rangle}{\partial t} = \nabla\cdot(\mathbf{K}_{eff}\cdot\nabla\langle T\rangle) \quad (22)$$

with

$$\langle\rho C_p\rangle = \epsilon_\beta(\rho C_p)_\beta + \epsilon_\sigma(\rho C_p)_\sigma$$

and a macroscopic thermal conductivity tensor of the form:

$$\mathbf{K}_{eff} = \epsilon_\beta\langle\mathbf{K}_\beta\rangle^\beta + \epsilon_\sigma\langle\mathbf{K}_\sigma\rangle^\sigma + \frac{\langle\mathbf{K}_\beta\rangle^\beta - \langle\mathbf{K}_\sigma\rangle^\sigma}{V}\cdot\int_{A_{\beta\sigma}}\mathbf{n}_{\beta\sigma}\mathbf{b}_\beta\,dA + \langle\tilde{\mathbf{K}}_\beta\cdot\nabla\mathbf{b}_\beta\rangle + \langle\tilde{\mathbf{K}}_\sigma\cdot\nabla\mathbf{b}_\sigma\rangle \quad (23)$$

where $\mathbf{b}_\beta$ and $\mathbf{b}_\sigma$ are the closure variables, i.e. the vector fields that map the local temperatures deviations to the gradient of the average temperature. They may be written as

$$\tilde{T}_\beta = \mathbf{b}_\beta\cdot\nabla\langle T\rangle + \Psi_\beta \quad (24)$$

$$\tilde{T}_\sigma = \mathbf{b}_\sigma\cdot\nabla\langle T\rangle + \Psi_\sigma \quad (25)$$

where $\Psi_\beta$ and $\Psi_\sigma$ are two constants (see [3]).

### 3.3.2. Closure problem

These two vector fields are solutions of the following quasi-static, integro-differential problem [3], in which periodic boundary conditions are assumed:

$$\nabla\cdot\tilde{\mathbf{K}}_\beta + \nabla\cdot(\mathbf{K}_\beta\cdot\nabla\mathbf{b}_\beta) = \epsilon_\beta^{-1}\mathbf{c}_\beta \quad \text{in the β-phase} \quad (26)$$

$$\nabla\cdot\tilde{\mathbf{K}}_\sigma + \nabla\cdot(\mathbf{K}_\sigma\cdot\nabla\mathbf{b}_\sigma) = \epsilon_\sigma^{-1}\mathbf{c}_\sigma \quad \text{in the σ-phase} \quad (27)$$

$$\mathbf{b}_\beta = \mathbf{b}_\sigma \quad \text{on } A_{\beta\sigma} \quad (28)$$

$$\mathbf{n}_{\beta\sigma}\cdot\mathbf{K}_\beta\cdot\nabla\mathbf{b}_\beta = \mathbf{n}_{\beta\sigma}\cdot\mathbf{K}_\sigma\cdot\nabla\mathbf{b}_\sigma + \mathbf{n}_{\beta\sigma}\cdot(\mathbf{K}_\sigma - \mathbf{K}_\beta) \quad \text{on } A_{\beta\sigma} \quad (29)$$

$$\mathbf{b}_\beta(\mathbf{r}+l_i) = \mathbf{b}_\beta(\mathbf{r}), \mathbf{b}_\sigma(\mathbf{r}+l_i) = \mathbf{b}_\sigma(\mathbf{r}), \quad i=1,2,3 \quad (30)$$

$$\langle\mathbf{b}_\beta\rangle = 0, \quad \langle\mathbf{b}_\sigma\rangle = 0 \quad (31)$$

Integral constant $\mathbf{c}_\beta$ and $\mathbf{c}_\sigma$ are given by

$$\mathbf{c}_\beta = \frac{1}{V}\int_{A_{\beta\sigma}}\mathbf{n}_{\beta\sigma}\cdot(\mathbf{K}_\beta + \mathbf{K}_\beta\cdot\nabla\mathbf{b}_\beta)\,dA \quad (32)$$

$$\mathbf{c}_\sigma = -\frac{1}{V}\int_{A_{\beta\sigma}}\mathbf{n}_{\beta\sigma}\cdot(\mathbf{K}_\sigma + \mathbf{K}_\sigma\cdot\nabla\mathbf{b}_\sigma)\,dA \quad (33)$$

Recalling the boundary condition (29), we see that there remains only one integral constant since $\mathbf{c}_\beta = -\mathbf{c}_\sigma$.

In the original paper of Nozad [4], integral terms $\mathbf{c}_\beta$ and $\mathbf{c}_\sigma$ are neglected, and the closure problem becomes much more simple. However we keep them for completeness as [3] proposed a simple way to compute them.

Indeed if one introduces two new vector fields $\mathbf{b}^*_\beta$ and $\mathbf{b}^*_\sigma$ and two scalar fields $B_\beta$ and $B_\sigma$ defined as

$$\mathbf{b}_\beta = \mathbf{b}^*_\beta + \mathbf{c}_\beta B_\beta \tag{34}$$

and

$$\mathbf{b}_\sigma = \mathbf{b}^*_\sigma + \mathbf{c}_\beta B_\sigma \tag{35}$$

then the closure problem (Eqs. (26)–(31)) may be rewritten into the two following differential problems:

**Problem 1**

$$\nabla\cdot\tilde{\mathbf{K}}_\beta + \nabla\cdot\left(\mathbf{K}_\beta\cdot\nabla\mathbf{b}^*_\beta\right) = 0 \quad \text{in the } \beta\text{-phase} \tag{36}$$

$$\nabla\cdot\tilde{\mathbf{K}}_\sigma + \nabla\cdot\left(\mathbf{K}_\sigma\cdot\nabla\mathbf{b}^*_\sigma\right) = 0 \quad \text{in the } \sigma\text{-phase} \tag{37}$$

$$\mathbf{b}^*_\beta = \mathbf{b}^*_\sigma \quad \text{on } A_{\beta\sigma} \tag{38}$$

$$\mathbf{n}_{\beta\sigma}\cdot\mathbf{K}_\beta\cdot\nabla\mathbf{b}^*_\beta = \mathbf{n}_{\beta\sigma}\cdot\mathbf{K}_\sigma\cdot\nabla\mathbf{b}^*_\sigma + \mathbf{n}_{\beta\sigma}\cdot(\mathbf{K}_\sigma-\mathbf{K}_\beta) \quad \text{on } A_{\beta\sigma} \tag{39}$$

$$\mathbf{b}^*_\beta(\mathbf{r}+l_i) = \mathbf{b}^*_\beta(\mathbf{r}), \mathbf{b}^*_\sigma(\mathbf{r}+l_i) = \mathbf{b}^*_\sigma(\mathbf{r}), \quad i=1,2,3 \tag{40}$$

**Problem 2**

$$\nabla\cdot(\mathbf{K}_\beta\cdot\nabla B_\beta) - \epsilon_\beta^{-1} = 0 \quad \text{in the } \beta\text{-phase} \tag{41}$$

$$\nabla\cdot(\mathbf{K}_\sigma\cdot\nabla B_\sigma) + \epsilon_\sigma^{-1} = 0 \quad \text{in the } \sigma\text{-phase} \tag{42}$$

$$B_\beta = B_\sigma \quad \text{on } A_{\beta\sigma} \tag{43}$$

$$\mathbf{n}_{\beta\sigma}\cdot\mathbf{K}_\beta\cdot\nabla B_\beta = \mathbf{n}_{\beta\sigma}\cdot\mathbf{K}_\sigma\cdot\nabla B_\sigma \quad \text{on } A_{\beta\sigma} \tag{44}$$

$$B_\beta(\mathbf{r}+l_i) = B_\beta(\mathbf{r}), B_\sigma(\mathbf{r}+l_i) = B_\sigma(\mathbf{r}), \quad i=1,2,3 \tag{45}$$

Therefore the integral constant may be computed by using the constraints (31):

$$\mathbf{c}_\beta = -\frac{\left\langle\mathbf{b}^*_\beta\right\rangle^\beta}{\left\langle B_\beta\right\rangle^\beta} = -\frac{\langle\mathbf{b}^*_\sigma\rangle^\sigma}{\langle B_\sigma\rangle^\sigma} \tag{46}$$

### 3.4. Numerical methods

In order to solve the closure problems (Eqs. (36)–(45)), the discretization scheme should respect flux conservation property and must be able to deal with non-diagonal or full tensor equations that arise due to wood fibre local conductivity orthotropy. This condition discards the classical 7-points finite volume scheme. We propose here a method based on a flux continuous and locally conservative finite volume scheme presented by Edwards and Rogers [29], but generalized to 3D problems. The principal steps of the discretization method are given here.

Considering a regular cartesian grid, the integration of the diffusive operator $\nabla\cdot(\mathbf{K}\cdot\nabla\mathbf{b})$ over a cell of volume $V$ and surface $\partial V$ for a component $b$ of the vector $\mathbf{b}$ may be expressed as

$$\begin{aligned}
&\frac{1}{V}\int_V(\nabla\cdot(\mathbf{K}\cdot\nabla b))\,\mathrm{d}V\\
&=\frac{1}{V}\oint_{\partial V}(\mathbf{n}\cdot(\mathbf{K}\cdot\nabla b))\,\mathrm{d}S\\
&=\frac{1}{\delta x}\left(K_{xx}\frac{\partial b\left(i+\frac12,j,k\right)}{\partial x}+K_{xy}\frac{\partial b\left(i+\frac12,j,k\right)}{\partial y}\right.\\
&\quad\left.+K_{xz}\frac{\partial b\left(i+\frac12,j,k\right)}{\partial z}\right)\\
&\quad-\frac{1}{\delta x}\left(K_{xx}\frac{\partial b\left(i-\frac12,j,k\right)}{\partial x}+K_{xy}\frac{\partial b\left(i-\frac12,j,k\right)}{\partial y}\right.\\
&\quad\left.+K_{xz}\frac{\partial b\left(i-\frac12,j,k\right)}{\partial z}\right)\\
&\quad+\frac{1}{\delta y}\left(K_{yx}\frac{\partial b\left(i,j+\frac12,k\right)}{\partial x}+K_{yy}\frac{\partial b\left(i,j+\frac12,k\right)}{\partial y}\right.\\
&\quad\left.+K_{yz}\frac{\partial b\left(i,j+\frac12,k\right)}{\partial z}\right)\\
&\quad-\frac{1}{\delta y}\left(K_{yx}\frac{\partial b\left(i,j-\frac12,k\right)}{\partial x}+K_{yy}\frac{\partial b\left(i,j-\frac12,k\right)}{\partial y}\right.\\
&\quad\left.+K_{yz}\frac{\partial b\left(i,j-\frac12,k\right)}{\partial z}\right)\\
&\quad+\frac{1}{\delta z}\left(K_{zx}\frac{\partial b\left(i,j,k+\frac12\right)}{\partial x}+K_{zy}\frac{\partial b\left(i,j,k+\frac12\right)}{\partial y}\right.\\
&\quad\left.+K_{zz}\frac{\partial b\left(i,j,k+\frac12\right)}{\partial z}\right)\\
&\quad-\frac{1}{\delta z}\left(K_{zx}\frac{\partial b\left(i,j,k-\frac12\right)}{\partial x}+K_{zy}\frac{\partial b\left(i,j,k-\frac12\right)}{\partial y}\right.\\
&\quad\left.+K_{zz}\frac{\partial b\left(i,j,k-\frac12\right)}{\partial z}\right)
\end{aligned} \tag{47}$$

Here $\mathbf{K}$ is supposed piecewise constant over each cell, although great variations may appear at the interfaces. The notation $K_{xy}$ is thus used for $K_{xy}(i,j,k)$.

The estimation of the three components of the gradient of $b$ is the main difficulty in the full tensor discretization. The idea is to divide a cell into eight sub-cells in which the closure variable is supposed to vary linearly, so that $b$ may be expressed in each sub-cell as

$$b = G_x x + G_y y + G_z z + G \tag{48}$$

Then, the gradient components in a sub-cell, $G_x$, $G_y$ and $G_z$ are easily expressed as a function of the values of the three closure variables at the sub-cell interfaces and the one at the cell center. For example, if we consider the sub-cell with positive coordinates relative to the cell center $C(i,j,k)$ (see Fig. 12), and if we note the points on this sub-cell interface as $I(i+\frac12, j+\frac14, k+\frac14)$, $J(i+\frac14, j+\frac12, k+\frac14)$ and $K(i+\frac14, j+\frac14, k+\frac12)$, then the expressions of the three spatial derivatives of $b$ are given by

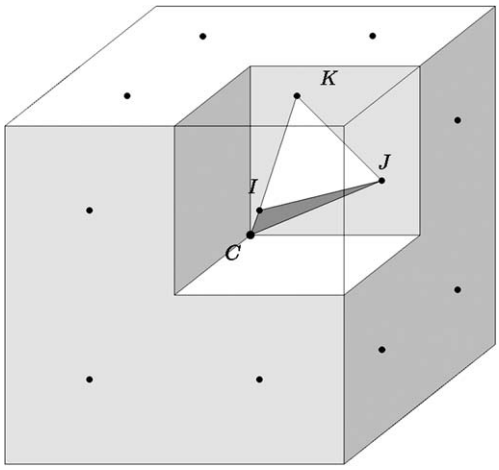


Fig. 12. Positions of the closures variables on the sub-cell interfaces.

$$\frac{\partial b}{\partial x} = G_x = \frac{1}{\delta x}(3b(I) - b(J) - b(K) - b(C)) \quad (49)$$

$$\frac{\partial b}{\partial y} = G_y = \frac{1}{\delta y}(-3b(I) + b(J) - b(K) - b(C)) \quad (50)$$

$$\frac{\partial b}{\partial z} = G_z = \frac{1}{\delta z}(-3b(I) - b(J) + b(K) - b(C)) \quad (51)$$

The continuity of the closure variables (28) is here implicit since the same variable is used at the interface between two cells. The last step in the discretization is to get an expression of the gradient components in terms of the closure variables at cell centers only. Substitution of the gradient expressions (49)–(51) into the flux continuity condition (29) for the 3 interfaces of a sub-cell, leads to a linear system of 12 equations, linking closure variables at cell center and interfaces. Resolution of this $(12 \times 12)$ linear system is done numerically by gaussian elimination and provides an expression of the gradients at the sub-cell interfaces as a function of cell center closure variables. The same work is done for each sub-cell, leading to the searched expression of the flux through the cell faces. This scheme requires 27 points for a full tensor equation discretization. The linear systems resulting from the closure problems discretization are solved with a preconditioned Bi-Conjugate Gradient Stabilized algorithm [30].

### 3.5. Results

#### 3.5.1. Effect of fibres homogenization

Some assumptions introduced by the wood fibres homogenization model (especially the square section and the constant porosity of the fibres) may seems disputable. In order to estimate the influence of the wood fibres homogenization over the macroscopic thermal conductivity, two computations are realised over a high resolution image (4.91 μm/pixel) of the wood insulator material, with filled and non-filled lumens:

- Sample 1: 0.26 $mm^3$ $(192 \times 192 \times 64$ voxels), with non-filled lumen
- Sample 2: 0.26 $mm^3$ $(192 \times 192 \times 64$ voxels), with filled lumens

The real thermal conductivity is affected to the wood cell-wall of sample 1, and the homogenized conductivity value is affected on the filled fibres of sample 2. The total porosity (i.e. the sum of the fibres porosity and outer porosity) is also provided for the sample 1. The measured fibres porosity is of 23% for this sample, which is slightly lower than the mean fibres porosity measured on larger volumes. In this case, the values of the homogenized conductivity, calculated with Eqs. (3) and (4), are $K_{long} = 0.68\ W\ m^{-1}\ K^{-1}$ and $K_{trans} = 0.32\ W\ m^{-1}\ K^{-1}$. The results summarized in Table 1 show that the wood fibres homogenization process tends to slightly increase the effective conductivity. The relative difference between the thermal conductivity tensor components of samples 1 and 2 is at most 8%. Given the complexity of the wood fibres geometry, it is remarkable that the simple model used to calculate the effective thermal conductivity of wood fibres gives such a good agreement. We can now be confident that the use of homogenized fibres does not affect notably the computed results.

#### 3.5.2. Influence of thermal contact resistance

Although the contacts between the fibres are often punctual, the modelisation does not take into account the possible thermal interfacial barriers. Indeed, in order to do so, we should be able to identify the contacts, thus a prior segmentation of the fibres is necessary. This segmentation

Table 1
Numerical results for two samples with homogenized and non-homogenized wood fibres

| | Macroscopic thermal conductivity tensor $\times 10^{-2}\ W\ m^{-1}\ K^{-1}$ | Porosity |
|---|---|---|
| Sample 1 (non-filled fibres) 0.26 $mm^3$ $(0.94 \times 0.94 \times 0.3\ mm^3)$ | $\begin{bmatrix} \mathbf{8.2} & 0.13 & -0.08 \\ 0.13 & \mathbf{7.7} & 0.08 \\ -0.08 & 0.08 & \mathbf{4.7} \end{bmatrix}$ | 74% (total porosity: 80%) |
| Sample 2 (filled fibres) 0.26 $mm^3$ $(0.94 \times 0.94 \times 0.3\ mm^3)$ | $\begin{bmatrix} \mathbf{8.6} & 0.21 & -0.03 \\ 0.2 & \mathbf{8.4} & 0.05 \\ -0.03 & 0.05 & \mathbf{5.1} \end{bmatrix}$ | 74% |

step is a very complex task for this kind of materials and is still a work in progress.

In order to give an order of magnitude of such thermal barriers, computations are realised on 2D images of $128 \times 128$ voxels representing a transverse and a longitudinal section of an intersection of two fibres, as shown in Fig. 13. The thermal contact resistance is modelled as a thin air layer of one pixel thickness. Its value is therefore overestimated here, because the two fibres are totally separated by the air layer. In this example, the porosity of the images is close to the real porosity of the sample (about 90%) and the conductivity tensor is as calculated in paragraph 3.1. The results of these simple tests show that the relative difference between the effective conductivities with or without thermal barrier is at most 2%. Neglecting the effect of thermal contact resistance has therefore very little influence on the heat transfer process considered.

### 3.5.3. Computation of the effective thermal conductivity of fibrous insulators

The effective thermal conductivity tensor of the wood/polymer composite material is computed for different averaging volume sizes within a 3D image with filled and homogenized fibres at a resolution of 19.64 μm/pixel:

- Sample 3: 1 $mm^3$ ($64 \times 64 \times 32$ voxels)
- Sample 4: 4 $mm^3$ ($128 \times 128 \times 32$ voxels)
- Sample 5: 13.4 $mm^3$ ($192 \times 192 \times 48$ voxels)
- Sample 6: 17.9 $mm^3$ ($192 \times 192 \times 64$ voxels)

The size of the estimated REV for geometrical and morphological properties is 13.4 $mm^3$. Low resolution images are so chosen to make the numerical computations. It should be stressed that, if the connectivity of the fibres network and the porosity may be conserved from a resolution to another, then the discretization will have a negligible effect over the computed macroscopic conductivity. Furthermore, tests on simple 2D images tend to show that the discretization does not modify the macroscopic results in a very sensible way, as long as the connectivity and porosity remain close.

Table 2 sums up the results and provides theoretical highest and lowest bounds for parallel and serial fibres arrangement, calculated with the measured sample porosity and wood fibres porosity. These bounds are given by

$$k_{\text{parallel}} = \epsilon_{\text{air}} k_{\text{air}} + \epsilon_{\text{fibres}} K_{\text{long}} \tag{52}$$

$$k_{\text{serial}} = \frac{k_{\text{air}} K_{\text{trans}}}{\epsilon_{\text{air}} K_{\text{trans}} + \epsilon_{\text{fibres}} k_{\text{air}}} \tag{53}$$

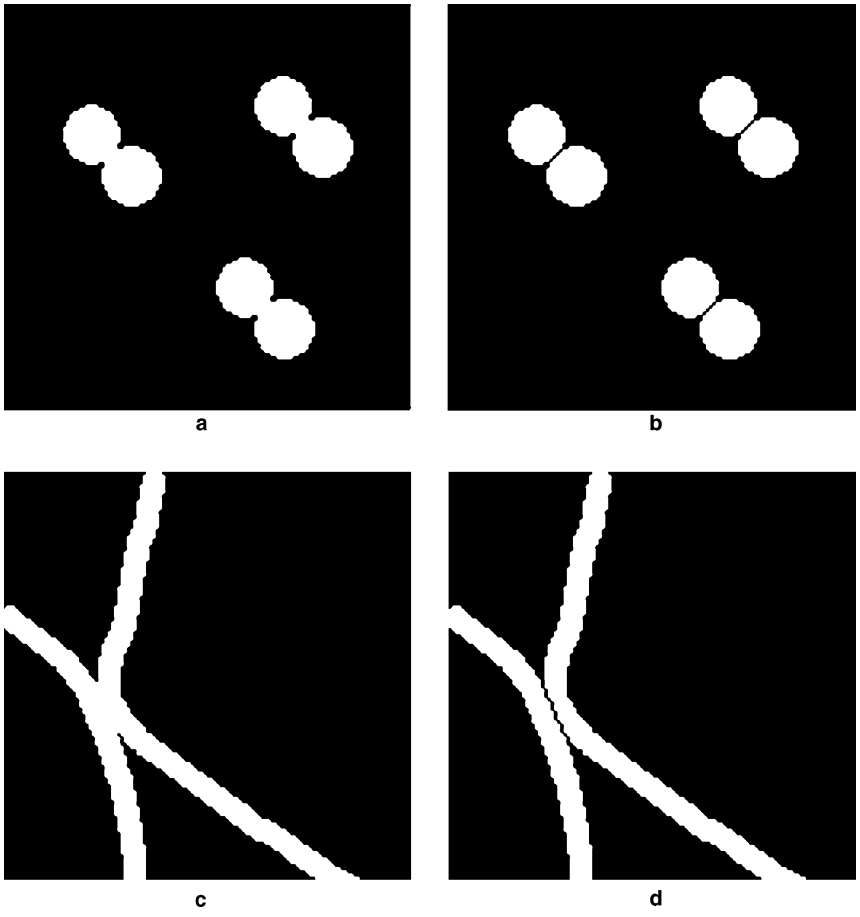


Fig. 13. Two configurations for testing the influence of interfacial thermal barriers: images (a) and (b) correspond to a transverse section and images (c) and (d) correspond to a longitudinal section.

Table 2
Numerical results and available experimental data for the wood/polymer fibres insulator

| | Macroscopic thermal conductivity tensor $\times 10^{-2}$ W m$^{-1}$ K$^{-1}$ | Porosity | Lowest bound $\times 10^{-2}$ W m$^{-1}$ K$^{-1}$ | Highest bound $\times 10^{-2}$ W m$^{-1}$ K$^{-1}$ |
|---|---|---|---|---|
| Sample 3: 1 mm$^3$ ($1.3 \times 1.3 \times 0.6$ mm$^3$) | $\begin{bmatrix} \mathbf{3.6} & -0.17 & 0.05 \\ -0.17 & \mathbf{2.9} & -0.04 \\ 0.05 & -0.03 & \mathbf{2.9} \end{bmatrix}$ | 96% | 2.7 | 5.3 |
| Sample 4: 4 mm$^3$ ($2.5 \times 2.5 \times 0.6$ mm$^3$) | $\begin{bmatrix} \mathbf{4} & -0.26 & 0.06 \\ -0.26 & \mathbf{3.3} & -0.08 \\ 0.06 & -0.08 & \mathbf{3.1} \end{bmatrix}$ | 94% | 2.7 | 6.4 |
| Sample 5: 13.4 mm$^3$ ($3.8 \times 3.8 \times 0.93$ mm$^3$) | $\begin{bmatrix} \mathbf{4.1} & -0.18 & 0.03 \\ -0.18 & \mathbf{3.5} & -0.04 \\ 0.03 & -0.08 & \mathbf{3.1} \end{bmatrix}$ | 93.5% | 2.8 | 6.7 |
| Sample 6: 17.9 mm$^3$ ($3.8 \times 3.8 \times 1.3$ mm$^3$) | $\begin{bmatrix} \mathbf{4} & -0.13 & 0.03 \\ -0.13 & \mathbf{3.5} & -0.04 \\ 0.03 & -0.08 & \mathbf{3.1} \end{bmatrix}$ | 93.8% | 2.8 | 6.5 |
| Hot-wire experimental data (isotropic assumption) | $\begin{bmatrix} \mathbf{5} & 0 & 0 \\ 0 & \mathbf{5} & 0 \\ 0 & 0 & \mathbf{5} \end{bmatrix} \pm 10\%$ | | n/a | |

The available experimental values come from measurements realized by the hot-wire method [16]. The hot-wire was put in longitudinal and transverse directions of the sample, i.e. planes respectively parallel and perpendicular to the sample surface, but no anisotropy was detected by the measures. The isotropy of the sample was then assumed in the identification process. It seems that the anisotropy is, in this case, too small to be detected by the experimental device. The experimental hot-wire values should so be taken as a basis for an order of magnitude comparison with the numerical values.

The computed thermal conductivities show only very small variations from a volume of 4 mm$^3$, which is slightly smaller that the REV established in the first part of this paper. This is not surprising, since this volume corresponds to the stabilization of the porosity, which is a key parameter, in these materials, that influence the effective thermal conductivity. Furthermore, the granulometric curves are not too far from the stabilized curves (see Figs. 5 and 6). It is however interesting to notice that this volume contains approximatively one correlation length in the transverse direction $Oz$, which is a strong indication that this material may be treated as a stratified medium.

The results are in agreement with the order of magnitude of the experimental data and the microstructure geometric anisotropy is correctly reflected in the computed conductivity tensor components. It should be stressed that the time-scales related to the experimental measurements remain small (about 5 min), so that the local thermal equilibrium may not always be achieved. Although this assumption must be validated, it might explain the slight differences between experimental and numerical values [31].

On a second series of numerical computations (Table 3), the other wood based insulator is considered. It was found that the size of the averaging volume is smaller for this material, which is related to its higher density. Indeed a volume size of approximatively 1.1 ($1.9 \times 1.9 \times 0.3$) mm$^3$ seems to be sufficiently representative regarding the morphological properties. This allows to work on images with higher resolutions. In a similar way as above, computations are done on increasing volume sizes, within an image featuring a 9.82 μm/pixel resolution. The stratified structure of this material allows to work on thin samples of 0.3 mm thickness:

- Sample 7: 0.5 mm$^3$ ($128 \times 128 \times 32$ voxels)
- Sample 8: 1.1 mm$^3$ ($192 \times 192 \times 32$ voxels)
- Sample 9: 2 mm$^3$ ($256 \times 256 \times 32$ voxels)

The experimental data available concerning this material are obtained from a combined hot-strip and hot-wire method described in [16], which allows the identification of the thermal conductivity of orthotropic materials. The hot-wire device is used to identify the longitudinal conductivity, while the hot-strip device is used for the transverse conductivity identification. It is interesting to note that the observation time scales involved when using the hot-strip device are greater than for the hot-wire one (up to 20 minutes), so thermal equilibrium is more likely to occur and the experimental transverse conductivity should be closer to the computed one.

It appears from the numerical results on samples 7, 8 and 9 that the computed thermal effective conductivity values remain very close from a size of an averaging

Table 3
Numerical results and available experimental data for the wood fibres insulator

| | Macroscopic thermal conductivity tensor $\times 10^{-2}$ W m$^{-1}$ K$^{-1}$ | Porosity | Lowest bound $\times 10^{-2}$ W m$^{-1}$ K$^{-1}$ | Highest bound $\times 10^{-2}$ W m$^{-1}$ K$^{-1}$ |
|---|---|---|---|---|
| Sample 7: 0.5 mm$^3$ ($1.3 \times 1.3 \times 0.3$ mm$^3$) | $\begin{bmatrix} \mathbf{6.9} & 0.09 & -0.005 \\ 0.09 & \mathbf{6.7} & 0.11 \\ -0.005 & 0.11 & \mathbf{4.9} \end{bmatrix}$ | 77% | 3.3 | 17.2 |
| Sample 8: 1.1 mm$^3$ ($1.9 \times 1.9 \times 0.3$ mm$^3$) | $\begin{bmatrix} \mathbf{7.8} & 0.03 & 0.007 \\ 0.03 & \mathbf{7.1} & 0.15 \\ 0.007 & 0.15 & \mathbf{5.2} \end{bmatrix}$ | 75% | 3.4 | 18.5 |
| Sample 9: 2 mm$^3$ ($2.5 \times 2.5 \times 0.3$ mm$^3$) | $\begin{bmatrix} \mathbf{7.6} & 0.00 & 0.01 \\ 0.01 & \mathbf{7.0} & 0.19 \\ 0.01 & 0.19 & \mathbf{5.2} \end{bmatrix}$ | 75% | 3.4 | 18.5 |
| Combined hot-strip/hot-wire experimental data | $\begin{bmatrix} \mathbf{10.7} & 0 & 0 \\ 0 & \mathbf{10.7} & 0 \\ 0 & 0 & \mathbf{5.3} \end{bmatrix} \pm 10\%$ | | n/a | |

volume larger than 1.1 mm$^3$. Again, it seems that the size of the REV was correctly estimated by the morphological analysis. Moreover, a very good agreement with the experimental transverse conductivity value is observed. In this case, the transverse thermal conductivity value is also available from the constructor and the given value of 0.042 W m$^{-1}$ K$^{-1}$ is still not far from our values. The computed longitudinal components values show, however, noteworthy differences (up to 34%) with the experimental data. As said previously, the hot-wire data give an order of magnitude for the expected values, so the numerical results may be considered satisfactory.

## 4. Conclusion

In this paper, we proposed a general approach to investigate the microstructure and compute the macroscopic thermal properties of real fibrous materials with the volume averaging technique. A thorough characterization of the microstructure is performed through 3D image analysis, using the mathematical morphology concepts. It is also shown that the morphological analysis provides a correct estimation of a REV. Furthermore, tools to detect and quantify structural and local anisotropy are presented, allowing the identification of the local thermal conductivity of wood fibres.

The numerical results are found to be of the same order of magnitude as the experimental values. In particular, the transverse conductivity of the wood insulator is very close to the data provided by the constructor and retrieved from the hot-strip method. These results hence tends to validate our approach. The difference observed between the hot-wire and numerical results may indeed be imputed to the lack of accuracy that arise in measures realized on heterogeneous media [31] and to the short time scales that may prevent the thermal equilibrium to be achieved. However, comparison with macroscopic temperature fields obtained by direct simulation should also be done in order to test the thermal equilibrium assumption, particularly in the case of periodic day/night thermal solicitations.

## Acknowledgements

The authors wish to thank Xavier Thibault for his help on the ID19 beam line at the ESRF. Our thanks also go to Fabien Cherblanc and Michel Quintard for their previous contributions to numerical implementation.

## References

[1] J.H. Cushman, L.S. Bennethum, B.X. Hu, A primer on upscaling tools for porous media, Adv. Water Resour. 25 (2002) 1043–1067.
[2] M. Quintard, S. Whitaker, Transport in ordered and disordered porous media: volume-averaged equations, closure problems and comparison with experiment, Chem. Eng. Sci. 48 (14) (1993) 2534–2537.
[3] S. Whitaker, The Method of Volume Averaging, Kluwer Academic Press, 1999.
[4] I. Nozad, R.G. Carbonell, S. Whitaker, Heat conduction in multiphase systems—i: Theory and experiment for two phase systems, Chem. Eng. Sci. 40 (5) (1985) 843–855.
[5] M. Kaviany, Principles of Heat Transfer in Porous Media, Mechanical Engineering, Springer-Verlag, 1991.
[6] S. Whitaker, Improved constraints for the principle of local thermal equilibrium, Ind. Eng. Chem. Prod. Res. Dev. 30 (1991) 983–997.
[7] M. Quintard, S. Whitaker, Local thermal equilibrium for transient heat conduction: theory and comparison with numerical experiments, Int. J. Heat Mass Transfer 38 (15) (1995) 2779–2796.
[8] C. Moyne, S. Didierjean, H. Amaral-Souto, O. Da Silveira, Thermal dispersion in porous media: one-equation model, Int. J. Heat Mass Transfer 43 (2000) 3853–3867.
[9] M. Quintard, S. Whitaker, One- and two-equation models for transient diffusion processes in two-phase systems, Adv. Heat Transfer 23 (1993) 369–464.
[10] F. Petit, F. Fichot, M. Quintard, Ecoulement diphasique en milieu poreux: modèle à non-équilibre local, Int. J. Therm. Sci. 38 (1999) 239–249.

[11] O. Coindreau, Etude 3D de préformes fibreuses: interaction entre phénomènes physicochimiques et géométrie, Ph.D. Thesis, Université Bordeaux I n° 2800, 2003.
[12] M. Coster, J.L. Chermant, Précis d'analyse d'image, Ed. du CNRS, 1985.
[13] G. Matheron, Eléments pour une théorie des milieux poreux, Masson, Paris, 1967.
[14] J. SerraImage Analysis and Mathematical Morphology, vol. 1, Academic Press, London, 1982.
[15] J. SerraImage Analysis and Mathematical Morphology: Theoretical Advances, vol. 2, Academic Press, London, 1988.
[16] C. Gobbé, S. Iserna, B. Ladevie, Hot strip method: application to thermal characterisation of orthotropic media, Int. J. Thermal Sci. 43 (2004) 951–958.
[17] M. Coster, J. Chermant, Image analysis and mathematical morphology for civil engineering materials, Cem. Conc. Compos. 23 (2001) 133–151.
[18] P. Salembier, J. Serra, Flat zones filtering, connected operators, and filters by reconstruction, IEEE Trans. Image Process. 4 (8) (1995) 1153–1160.
[19] P. Castéra, D. Jeulin, F. Bos, F. Michaud, C. Delisée, Of microstructural morphology on the macroscopic properties of cellulosic fibrous materials, in: Proceedings of the International Conference on Wood and wood fiber Composites, Stuttgart, Germany, 2000.
[20] A. Ahmadi, M. Quintard, Large-scale properties for two-phase flow in random porous media, J. Hydrol. 183 (1996) 69–99.
[21] M. Quintard, M. Kaviany, S. Whitaker, Two-medium treatment of heat transfer in porous media: numerical results for effective properties, Adv. Water Resour. 20 (1997) 77–94.
[22] M. Quintard, S. Whitaker, Transport in ordered and disordered porous media iv: computer generated porous media for three-dimensional systems, Transp. Porous Media 15 (1) (1994) 51–70.
[23] M. Quintard, S. Whitaker, Transport in ordered and disordered porous media v: geometrical results for two-dimensional systems, Transp. Porous Media 15 (2) (1994) 183–196.
[24] J.F. Siau, Transport Processes in Wood, in: Springer Series in Wood Science, 1984.
[25] R.K. Bhattacharyya, Heat-transfer model for fibrous insulations, in: D.L. McElroy, R.P. Tye (Eds.), Thermal Insulation Performance, American Society for Testing and Materials, 1980, pp. 272–286.
[26] G.W. Jackson, D.F. James, The permeability of fibrous porous media, Can. J. Chem. Eng. 64 (1986) 364–374.
[27] M. Özisik, Radiative Transfer and Interaction with Conduction and Convection, Wiley–Interscience Publication, 1973.
[28] F.A. Howes, S. Whitaker, The spatial averaging theorem revisited, Chem. Eng. Sci. 40 (8) (1985) 1387–1392.
[29] M. Edwards, C. Rogers, A flux continuous scheme for the full tensor pressure equation, in: Christie et al. (Eds.), Proceedings of the 4th European Conference on the Mathematics of Oil Recovery, Norway, June 1994.
[30] H.A. Van der Vorst, Bi-CGSTAB: a fast and smoothly converging variant of BI-CG for the solution of nonsymmetric linear systems, SIAM J. Sci Statist. Comput. 13 (1992) 631–644.
[31] G.C. Glatzmaier, W.F. Ramirez, Use of volume averaging for the modeling of thermal properties of porous materials, Chem. Eng. Sci. 43 (12) (1988) 3157–3169.